

The Application of Convolutional Neural Networks for Tomographic Reconstruction of Hyperspectral Images

Wei-Chih Huang,^{1,*} Mads Svanborg Peters,^{2,†} Mads Juul Ahlebaek,^{3,‡}
Mads Toudal Frandsen,^{1,§} René Lyng Eriksen,^{4,¶} and Bjarke Jørgensen^{2,||}

¹*CP³-Origins, University of Southern Denmark,
Campusvej 55 5230 Odense M, Denmark*

²*Newtec Engineering A/S, 5230 Odense, Denmark*

³*Department of Physics, Chemistry and Pharmacy*

⁴*Mads Clausen Institute, University of Southern Denmark,
Campusvej 55 5230 Odense M, Denmark*

(Dated: September 1, 2021)

Abstract

A novel method, utilizing convolutional neural networks (CNNs), is proposed to reconstruct hyperspectral cubes from computed tomography imaging spectrometer (CTIS) images. Current reconstruction algorithms are usually subject to long reconstruction times and mediocre precision in cases of a large number of spectral channels. The constructed CNNs deliver higher precision and shorter reconstruction time than a standard expectation maximization algorithm. In addition, the network can handle two different types of real-world images at the same time — specifically ColorChecker and carrot spectral images are considered. This work paves the way toward real-time reconstruction of hyperspectral cubes from CTIS images.

* huang@cp3.sdu.dk

† mape@newtec.dk

‡ maahl17@student.sdu.dk

§ frandsen@cp3.sdu.dk

¶ rle@mci.sdu.dk

|| bjarke@newtec.dk

I. INTRODUCTION

Hyperspectral imaging (HSI) [1], originating in earth observations and the launch of Landsat 1, has found several applications in control and quality assurance within the food industry. The acquired spectral information enable feature recognition, e.g. spectroscopic differentiation of materials [2], detection of foreign objects [3] and optical sorting [4]. Among the existing techniques of hyperspectral cube imaging, pushbroom (line scan) [5] is the most well-known.

Despite its ability to record images of moving objects in a broad range of wavelengths, the pushbroom system also has drawbacks: The first is that the velocity of imaged objects has to be known to high precision and any uncertainties will result in distortion of images and the second is the high cost of the equipment. That hinders broader applications of hyperspectral imaging.

On the other hand, the computed tomography imaging spectrometer (CTIS) [6–8] is a non-scanning snapshot HSI system, that is portable, cheaper and more compact than the pushbroom HSI system. It outputs a 2-dimensional (2-D) image of multiplexed spatio-spectral projections surrounding a direct image of the 3-D hyperspectral cube of the field stop-limited image scene. That is, the cube is projected into a 2-D image by superimposing the cube images in a wavelength-dependent way. CTIS has found several applications including remote sensing microbiology [9], ophthalmology [10], space surveillance and astronomy [11] as well as food and agricultural science [12, 13]. One specific food science application is the detection of frost damage in carrots that is not visible in standard color RGB images.

In Fig. 1a we show an example of a CTIS image of a ColorChecker Classic Mini (ColorChecker) captured with a custom-made CTIS camera, which utilizes the same optical system layout as White et al. in Ref. [14]. The CTIS image consists of a central zeroth-order undiffracted scene image and four surrounding first-order diffractions. As detailed in section II we create synthetic CTIS images for training the neural networks by using a reference $200 \times 400 \times 216$ (two spatial and one spectral dimension) hyperspectral cube of the ColorChecker and carrots acquired with a pushbroom HSI system. RGB visualizations (spectral channels 650, 550 and 470 nm) of the ColorChecker and carrots are shown in Fig. 1b and Fig. 1c, respectively, and a true RGB image of the ColorChecker is shown in

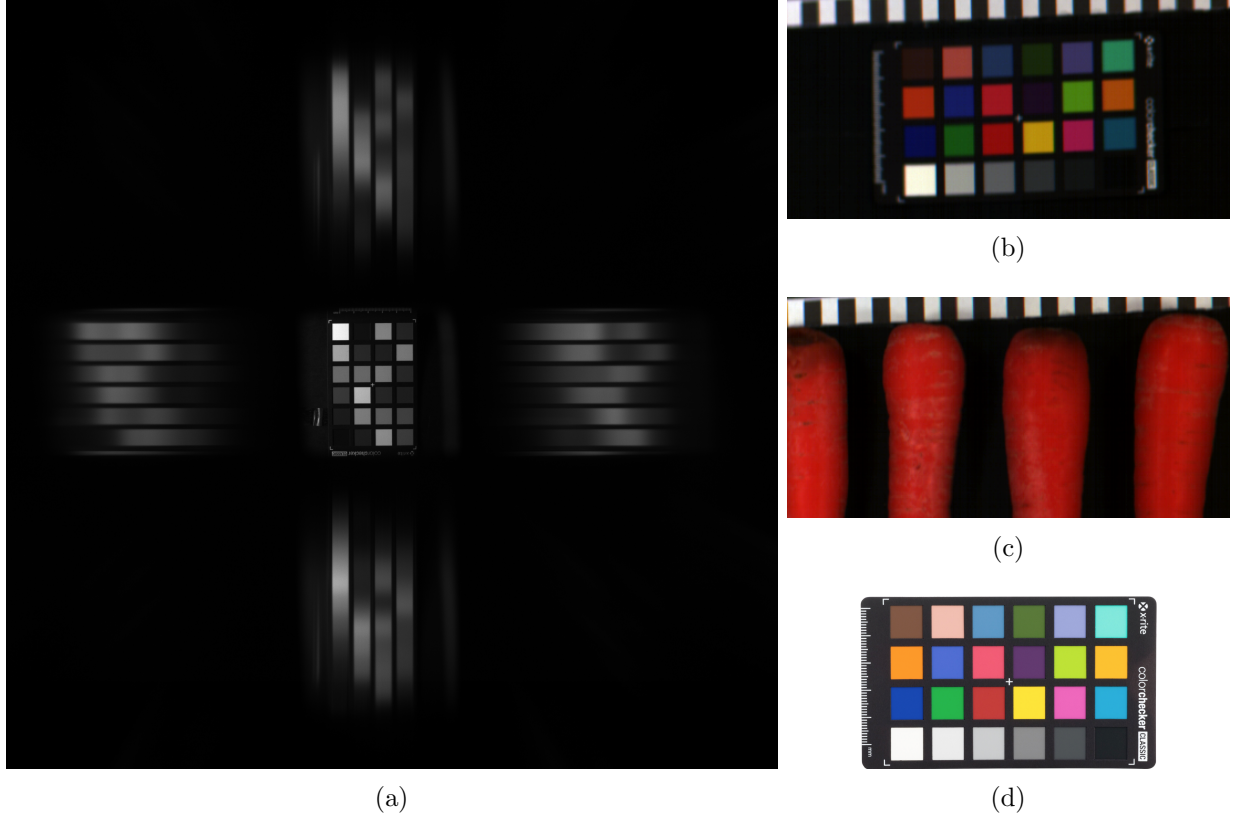


FIG. 1. (a) Experimental CTIS image of the ColorChecker acquired with a custom CTIS camera. RGB colorization of both hyperspectral cube of (b) the ColorChecker and (c) carrots acquired with the HSI system. (d) True RGB image of the ColorChecker.

Fig. 1d.

As CTIS images are compressed and not as easy to analyze as hyperspectral cubes, fast and precise real-time reconstruction of the hyperspectral cube from a CTIS image is an important but challenging goal. In practice, the common dimension of the hyperspectral cube often exceeds $100 \times 100 \times 100$, resulting in long reconstruction times and mediocre accuracy for existing algorithms [14–16]. Therefore, we consider neural networks to circumvent the limitations of current reconstruction algorithms. To the best of our knowledge it is the first time convolutional neural networks (CNNs) are used to reconstruct hyperspectral cubes from CTIS images.

Deep neural networks (DNNs), which can reproduce arbitrary functions given enough numbers of neurons and layers, are efficient at discovering underlying patterns and correlations among the input and output parameters. However, changing the order of input parameters leaves the output invariant — since an exchange of two or more input features can be compensated by swapping the corresponding weights in the following hidden layer.

Therefore DNNs are not ideal for processing images where interchanging pixels of an image may alter the image itself. Furthermore, for high-resolution images, the resulting number of input features, proportional to the number of the image pixels, is too large to cope with for DNNs. As a consequence, a new type of network, CNN, for image processing and recognition was proposed by LeCun et al [17, 18]. Common kernels (filters) are applied to input images for feature extraction such that one can significantly reduce the input dimensionality and capture the correlations among input features.

Since our goal is to reconstruct a hyperspectral cube comprised of images at different wavelengths from a CTIS image, both the input and output of the network are images. In this situation, it is natural to construct the network using only CNN layers, unlike tasks of image *classifications* where flattening to a 1-D vector after CNN layers and fully-connected layers are present. To construct our neural networks, we make use of **TensorFlow** [19], an end-to-end, open-source machine learning platform. It seamlessly incorporates **Keras** [20], a deep learning application programming interface written in **Python** [21].

II. DATA PREPARATION AND CNN ARCHITECTURE

In this Section, we start by detailing how the synthetic CTIS data are created and used in the network training. Next, we elucidate how the neural network is constructed in **Keras** and the strategies employed for training, validation and testing of the networks.

A. Synthetic CTIS Data Generation

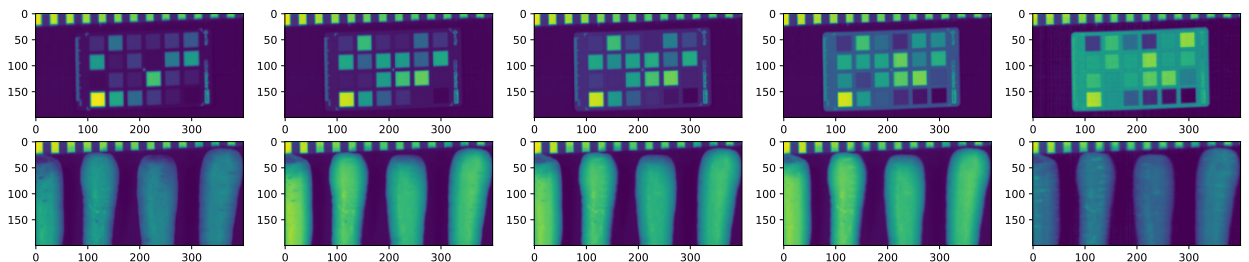


FIG. 2. Original spectral channels of the ColorChecker (top row) and carrots (bottom). The vertical and horizontal axes indicate the location of pixels. Each image corresponds to a single wavelength: from left to right, 603, 734, 770, 827, 969 nm, respectively. Instead of displaying grayscale images, the colormap of *viridis* is used to highlight variations in images.

As mentioned above, we use hyperspectral cubes of the ColorChecker and carrots, acquired by the pushbroom HSI system at our disposal. The pushbroom HSI system consists of a conveyor belt to translate the objects we image, i.e., the ColorChecker and carrots, four 150 W halogen lamps positioned above the conveyor belt and a hyperspectral pushbroom camera. The camera contains an ImSpector V10E spectrograph (Specim), a 50 mm C Series VIS-NIR objective (Edmund Optics) and a Qtechnology QT5022 computer vision system equipped with a CMOS CMV4000-E12 image sensor (CMOSIS). The pushbroom system captures 216 spectral channels ranging from 384-972 nm at a spatial resolution of approximately $0.33 \text{ mm pixels}^{-1}$. For illustration, five of the 216 spectral channels are displayed in the top and bottom row of Fig. 2 for the ColorChecker and carrots, respectively. We should emphasize that each image represents a specific *single* wavelength: from left to right, 603, 734, 770, 827, 969 nm, respectively. In other words, they are grayscale images, not standard color RGB images. The colormap of *viridis* is, however, employed to make variations in images more pronounced. The same colormap applies to all the following images.

To create synthetic CTIS images, we then randomly select five channels and crop each of them into smaller 100×100 pixel images, resulting in $30401 = (200 - 100 + 1) \times (400 - 100 + 1)$ different $100 \times 100 \times 5$ hyperspectral cubes. For each cropped hyperspectral cube, we superimpose the five channels, shown in the top row in Fig. 3a, with the wavelengths in ascending order from the left to right. The superimposing is done in a way to simulate the

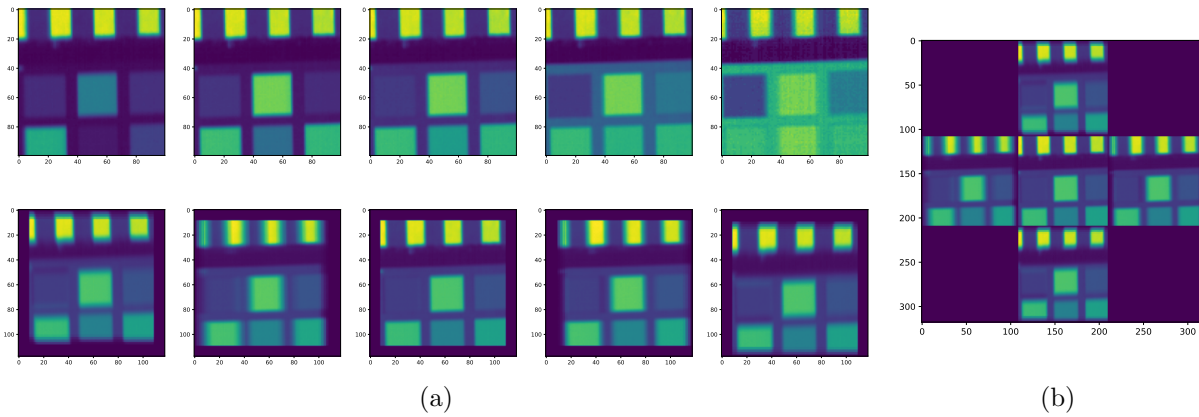


FIG. 3. (a) Five spectral 100×100 channels of the ColorChecker (top row) with corresponding blocks of the zeroth- and first-order diffraction blocks (bottom row). (b) Simulated CTIS image based on the five channels in (a).

CTIS diffraction image where channels of different wavelengths are shifted by a different

number of pixels as demonstrated in Fig. 3b. The central zeroth-order diffraction square in Fig. 3b is obtained by averaging over the five channels in the top row of Fig. 3a. The surrounding four first-order diffraction images are created in a similar way but with the five channels, from left to right in the top row of Fig. 3a, shifted in a certain direction by 1, 3, 5, 7, 9 pixels respectively. The top block above the central one, for example, features upward shifts, resulting in the elongated pattern along the vertical direction. The four black corners in the resulting image (Fig. 3b) are then removed and finally the diffraction image is divided into five block images shown in the bottom row of Fig. 3a. The five panels therein from left to right are simply the top, left, central, right and bottom blocks from Fig. 3b, respectively.

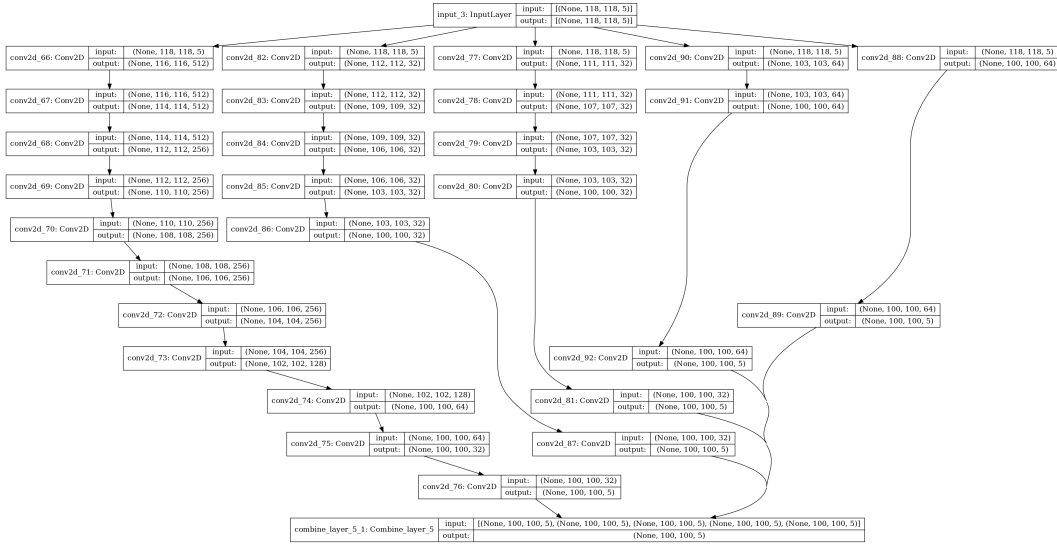


FIG. 4. CNN architecture for outputs of 5 spectral channels.

Our goal is now to train networks to reproduce the original five spectral channels from the synthetic CTIS images such as Fig. 3b. As a result, the corresponding bottom row of Fig. 3a comprises the input features of format (118, 118, 5), in which the first two entries in the parentheses correspond to the image dimension and the last one indicates the number of channels. The output target variables are simply original channels (top row) of format (100, 100, 5).

B. Network architecture, data preparation and network training

Since both the input and output are images, it is natural to utilize only 2-D convolutional layers, denoted by Conv2D in Keras, without applying flattening into a 1-D array

after the last layer of **Conv2D** as usually done in CNN image classifications. The network architecture is displayed in Fig. 4, where the top layer corresponds to the input layer and the dimensionality is specified by (None, 188, 188, 5). The symbol ‘None’ represents an undetermined batch size (number of samples in a single batch) that assumes the default value of 32 if not specified, and the following three entries denote the dimension of input images as explained above. The input layer is followed by five distinctive branches, each comprised of multiple **Conv2D** layers. In the end, each of these five branches outputs a hyperspectral cube of dimension (100, 100, 5). These five cubes are then concatenated and fed into the last customized layer **Combine_layer_5**. This layer yields a linear combination of the input cubes with bias parameters that has the same dimension of (100, 100, 5), matching that of the cropped hyperspectral cubes. The reason for having the five branches of different complexity is to mimic the methods of decision tree ensembles such as random forests [22] and boosted trees [23] where individual tree represents a weak learner but many of them are combined to make stable predictions and achieve good performance.

For all of **Conv2Ds**, the convolution kernel (filter) moves one pixel rightwards or downwards on a 2-D image between two successive applications of the kernel. The kernel size and the number of kernels for each **Conv2D** layer can be inferred from the difference in the image dimensions between the layer’s input and output. The first **Conv2D** in the first branch on the left, for instance, has 512 kernels of size (3, 3) (height, width) that convert the input of (118, 118, 5) into the output of (116, 116, 512) without padding (without adding zeros to the boundary of the image). For all of the last layers of the five branches, padding is used such that the dimensionality of channels is maintained. The network contains 6.79 million trainable parameters in total.

The data involved in the training process includes 2.4 million samples¹, created in three different ways: *full cropping*, *sparse cropping*, and *blank* images.

The *full cropping* image sample is created by taking *all* of 30401 possible cropped hyperspectral cubes of size $100 \times 100 \times 5$, given a $200 \times 400 \times 5$ hyperspectral cube (one with five specific wavelengths chosen from the original $200 \times 400 \times 216$ with 216 wavelengths). We repeat the process for several of randomly selected cubes of $200 \times 400 \times 5$.

The *sparse cropping* image sample is created by cropping only 217 cubes with a distance

¹To clarify, a sample consists of a single hyperspectral cube of $100 \times 100 \times 5$ (output) and the corresponding CTIS image (input).

of 10 (15) pixels between the nearby hyperspectral cubes along the vertical (horizontal) direction on 2-D images, i.e., $\text{strides} = (10, 15)$ for the cropping window. By doing so, the network is beneficially allowed to see many more different combinations of original hyperspectral cubes without incurring an enormous dataset. In fact, CNN has built-in partial translation invariance as a small translational shift in the input image have little or no impact on the output of latter or deeper CNN layers². As a consequence, we can afford a certain degree of sparsity in cropping. Note that there exists no overlap of the $100 \times 100 \times 5$ cubes used in full and sparse cropping.

Finally the *blank* image sample is created to avoid any bias originating from a specific image type – the ColorChecker – under consideration. We include samples with only zero pixel values to mitigate any residual patterns of error associated with the properties of the training cubes.

The 2.4 million samples are divided into the training (90%) and validation (10%) datasets. We shall test the model on extra, unseen datasets of 1 million new cubes of $100 \times 100 \times 5$ from both full and sparse cropping. Notice that the network has not seen the test data during training.

We use the mean squared error (MSE) for the loss function, that quantifies the difference between the network predictions and the true images, and the mean absolute error (MAE) as an independent metrics on errors:

$$\text{MSE} = \frac{1}{N} \sum_{i=1}^N (Y_i - \hat{Y}_i)^2, \quad \text{MAE} = \frac{1}{N} \sum_{i=1}^N |Y_i - \hat{Y}_i|, \quad (1)$$

where N is the data sample size, i labels the sample, \hat{Y}_i is the network prediction and Y_i is the true value. By comparison, MSE is more prone to outliers (those with large residual errors) due to the quadratic dependence on the residual while MAE tends to encourage more sparse error distributions, i.e., more vanishing residual errors among pixels in samples. The Adam algorithm [24], which is a method of stochastic gradient descent based on the adaptive estimation of first-order and second-order moments, is used to minimize the loss function during training. We choose a learning rate of 10^{-4} .

To prevent overfitting the training data, we make use of **callbacks**, which interrupts

²In light of dimension deduction of CNN layers without padding, a small part of the output of a deep CNN layer corresponds to a much larger portion of the original input image.

network training when the loss on the validation data ceases to improve and save the layer weights with the smallest value of the loss on the validation set. Overfitting occurs when a trained network performs very well on the data set that it was trained on but is not able to generalize to different data. It implies that the network is overtrained and undesirably learns noise or statistical fluctuations pertaining to the training data, rather than assimilating the underlying pattern.

III. RESULTS AND GENERALIZATIONS TO 25 SPECTRAL CHANNELS AND CARROT HYPERSPECTRAL CUBES

In this section, we begin with presenting the training results based on the generated data discussed above. Next, we take a step further to see if networks can handle a much more complicated task of decomposing CTIS images consisting of 25 100×100 images, an important step toward mimicking real-world hyperspectral cubes that usually have more than 100 spectral channels. Finally, we investigate if the model can manage a different type of hyperspectral cubes from synthetic CTIS images of carrots.

A. CNN predictions on ColorChecker images with 5 spectral channels

We train the network on four NVIDIA Tesla V100-SXM2-32GB GPUs running in parallel. After 40 epochs³ we reach $(\text{MSE}, \text{MAE}) \sim (0.6, 0.5)$ for the training data and $(1.0, 0.6)$ for the validation data. Given that the pixel value ranges from 0 to 255, such small residual errors indicate very good performance. As our synthetic data are divided into three categories, *full cropping*, *sparse cropping* and *blank images*, we also calculate the average errors for each of these categories as summarized in Table I. The network performs better on the full cropping data category as there exists a significant degree of overlap among the samples and thus less variation in this category and also due to (partial) translation invariance of CNN.

By contrast, samples from the sparse cropping category consist of many different combinations of the $200 \times 400 \times 5$ hyperspectral cubes, featuring much more variety so it becomes harder for the network to make correct predictions in this category. On the other hand, the

³An epoch refers to one iteration where the network sees the entire training dataset once.

| | MSE | MAE |
|-------------------------------------|----------------------|----------------------|
| Training data of full cropping | 0.16 | 0.30 |
| Training data of sparse cropping | 1.63 | 0.85 |
| Blank images | 4.5×10^{-3} | 5.2×10^{-2} |
| Unseen test data (full plus sparse) | 1.86 | 0.89 |

TABLE I. MSE and MAE for the entire training and test datasets. Data from sparse cropping have larger errors than full cropping, while the blank images, used to reduce the bias, have the smallest errors. The errors show the network generalizes very well to a completely new dataset, corroborated by similar values of MSE and MAE to those of the sparse cropping training data.

network attains consistent performance on the completely new CTIS images from both full and sparse cropping⁴. The corresponding values of MSE and MAE are similar to those of sparse cropping in the training data.

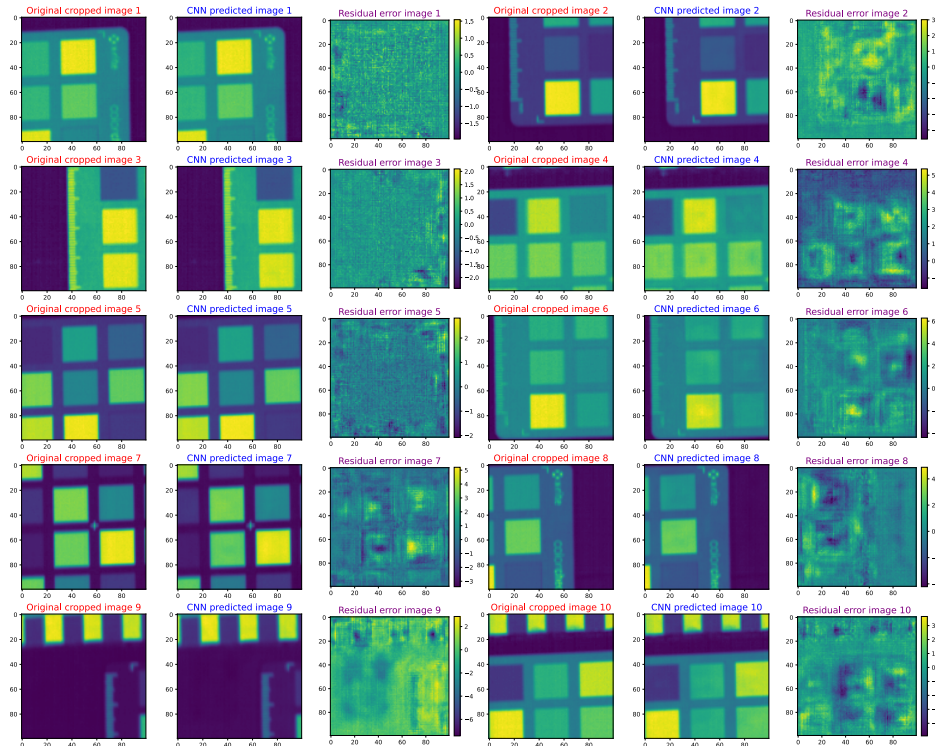


FIG. 5. Comparison between the original channels and CNN predictions for samples from training (three columns on the left) and test (three on right) datasets. Here, we show the comparison only for the third out of the five channels. For the residual error images, we add colorbars to indicate the absolute scale of errors where the ranges of the colorbars vary.

Fig. 5 shows a comparison between the CNN predictions and the original images for

⁴Note that the test data is generated based on completely distinct hyperspectral cubes from those of the training data. That is quite different from the usual practice, where training, validation and test data originate from the same source of data.

channel 3 of the five channels used. It illustrates the quantitative results of table I. The odd image indices (the first 3 columns from the left) label samples from the training datasets and the even indices (the last 3 columns) label samples from the test datasets. For both the training and test sets we display, from left to right, the original image of channel 3, the CNN prediction and the difference between the two. The samples in the first three rows are from the full cropping category and the last two rows are from the sparse category. It is evident that the residual error in the training data is quite small for the full cropping data category (top three panels of the third column) as compared to those of the sparse. The larger difference between the true and predicted pixel values, the more visible the residual error pattern, which is also indicated by larger ranges of error colorbars – for example, the residual errors for image 1 are smaller than those of image 6. It is also evident that the model generalizes well to the unseen samples (images with even indices).

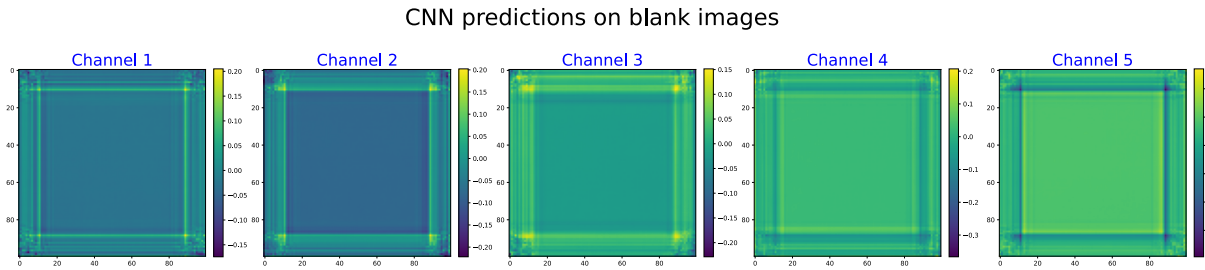


FIG. 6. Model predictions on the five spectral channels for blank input images. The residual errors are much smaller than the rest of the training data as shown in Table I. The crossing patterns around the corners could be attributable to the common rectangular shapes in the training data as well as square CNN kernels.

As mentioned above, to ensure that the network is free of bias because it only sees CTIS images of the ColorChecker, the samples of blank images are also included in the training data. In Fig. 6, the residual errors exhibit patterns of crossing at right angles especially around the four corners. These patterns could be attributed to the rectangular shapes of the ColorChecker and the square kernels applied in the CNN layers. The magnitude of the residual errors, nonetheless, are much smaller compared to those of the ColorChecker as can be seen in Table I.

Having demonstrated the network’s ability to reconstruct the hyperspectral cube from synthetic CTIS images of the ColorChecker with five wavelength channels, we want to consider the performance on different kinds of images – in particular images of practical relevance

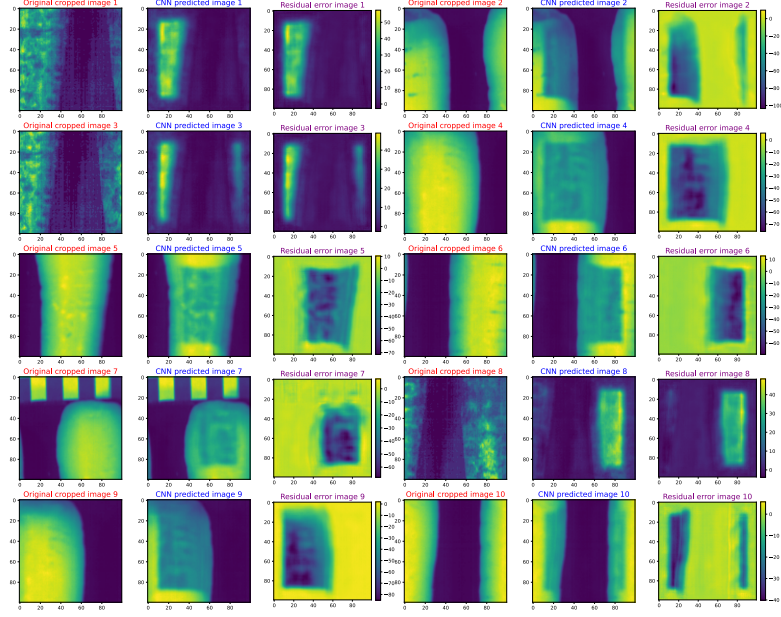


FIG. 7. Network predictions on wholly unseen carrot images. The network can capture the overall shapes but fall short of reconstructing details.

— as well as a larger number of output channels.

B. Predictions on carrot images

First we simply take the network trained on the ColorChecker images and apply it directly to reconstruct the hypercube from the synthetic CTIS images of carrots (bottom row of Fig. 2). The reason we choose carrot images is that the corresponding hyperspectral cubes can be used to detect frost damages in carrots [12]. The results are presented in Fig. 7. The model, overall, is able to capture the shape of carrots for the most part but fail to reproduce details precisely. In particular noticeable residual errors manifest themselves as approximate rectangles in dark blue. This is not surprising but can be ascribed to the bias inherited from ColorChecker images, which are basically comprised of rectangles.

IV. APPLYING CNNs TO OUTPUT OF 25 SPECTRAL CHANNELS FROM COLORCHECKER AND CARROT HYPERSPECTRAL CUBES

Now, we are in a position to tackle the more challenging task of reconstructing hyperspectral cubes with 25 spectral channels from synthetic CTIS images. We closely follow

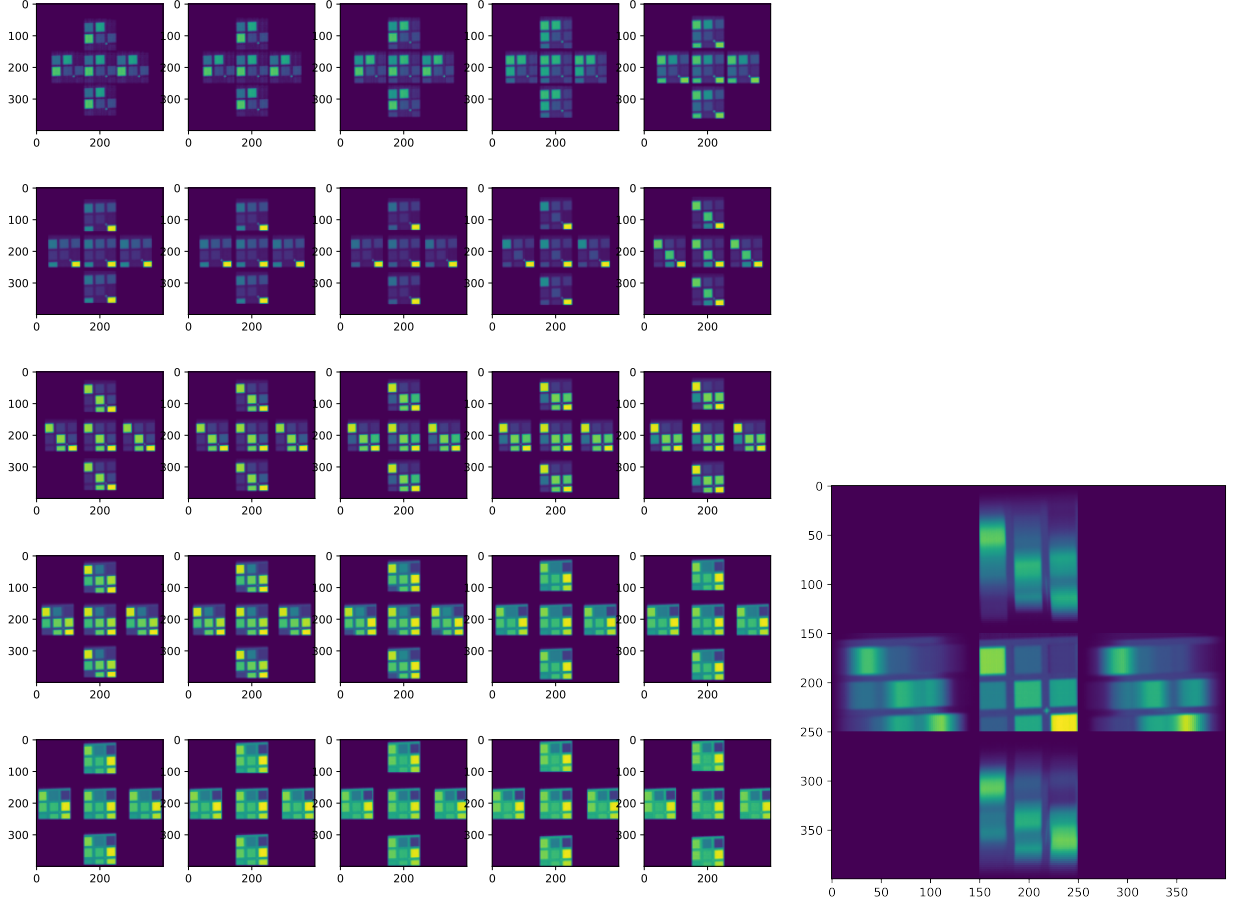


FIG. 8. Left panel: Cropped, diffraction images of the 25 spectral channels. Right panel: The resulting simulated CTIS image.

the procedure of data generation in Section II. To create a synthetic CTIS image, we take 25 channels from the original hyperspectral cube – obtained with the aforementioned push-broom system – and crop this $200 \times 400 \times 25$ hyperspectral cube into $100 \times 100 \times 25$ hyperspectral cubes. For each hyperspectral cube, the 25 channels are superimposed with shifts of $(2, 4, 6, \dots, 50)$ pixels for the first-order diffraction as shown in Fig. 8. The left panel shows the original channels while the right panel represents the resulting CTIS image. In this case, the input images become 200×200 , nearly three times larger than the previous one. As demonstrated above, it is more difficult for the network to make correct predictions on samples from sparse cropping than full cropping. Therefore, we focus only on the more challenging data from sparse cropping, consisting of half a million samples.

Due to the larger dimensionality (roughly three times larger) of input images and the higher number of output channels (five times more) for each sample, compared to the 5-

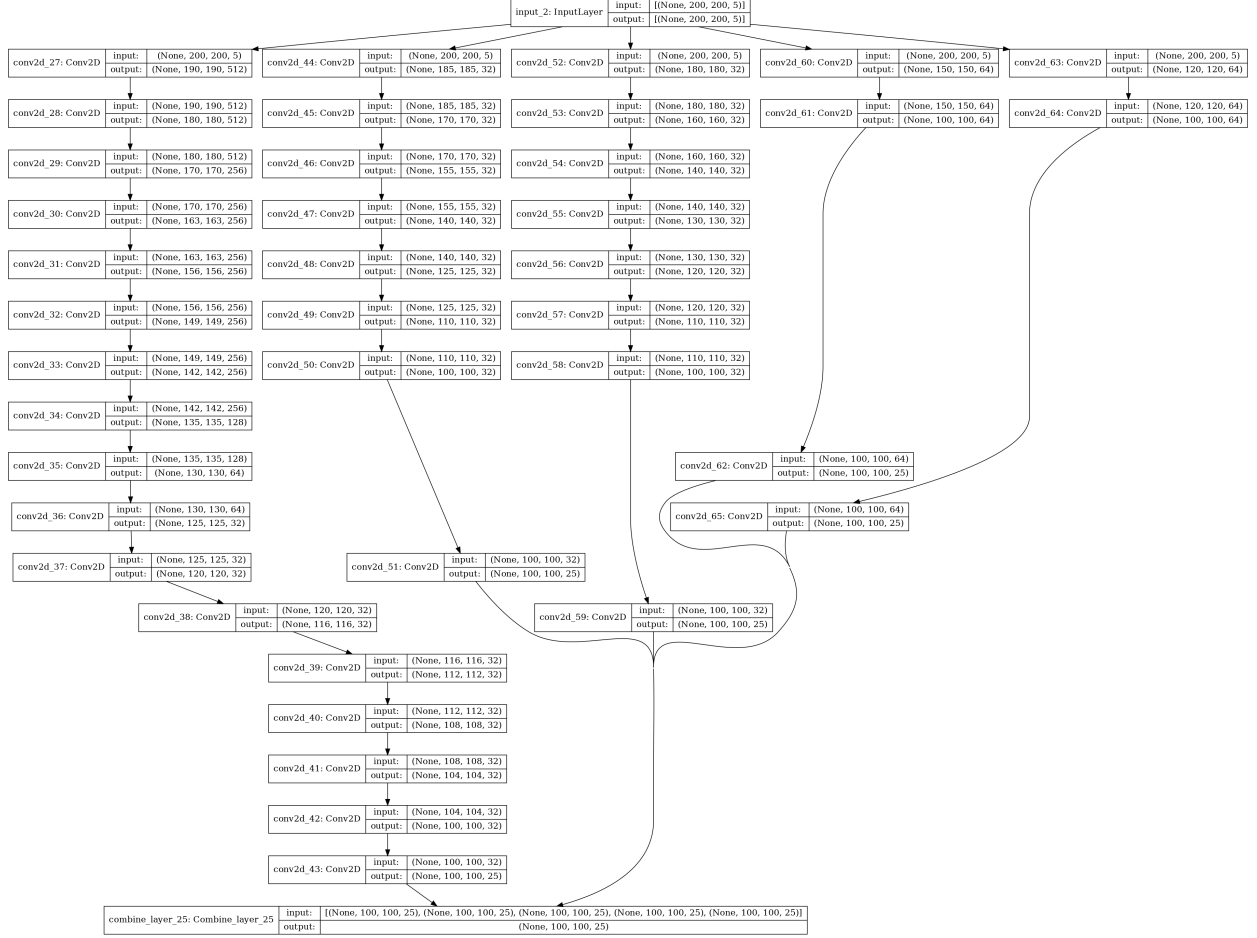


FIG. 9. CNN architecture for outputs of 25 spectral channels.

channel scenario, the second network shown in Fig. 9 becomes approximately twelve times bigger than before – 85.9 million trainable parameters in total versus 6.79 million for the first network. The comparison, similar to Fig. 5, between the true images and model predictions is displayed in Fig. 10a for the training (three columns on the left) and test (three on right) data. Clearly, the model also generalizes satisfactorily to completely unseen data with quite similar accuracy.

Finally, we include into the training data another 0.5 million samples of carrot images. The results are illustrated in Fig. 10b – the network is able to simultaneously deal with the different types of images very well with the decent ability of generalization.

The model performance is summarized in Table II which breaks down into two types of training data – the ColorChecker and the ColorChecker plus carrots. It is evident that the model can reproduce two different types of hyperspectral cubes but performs slightly better

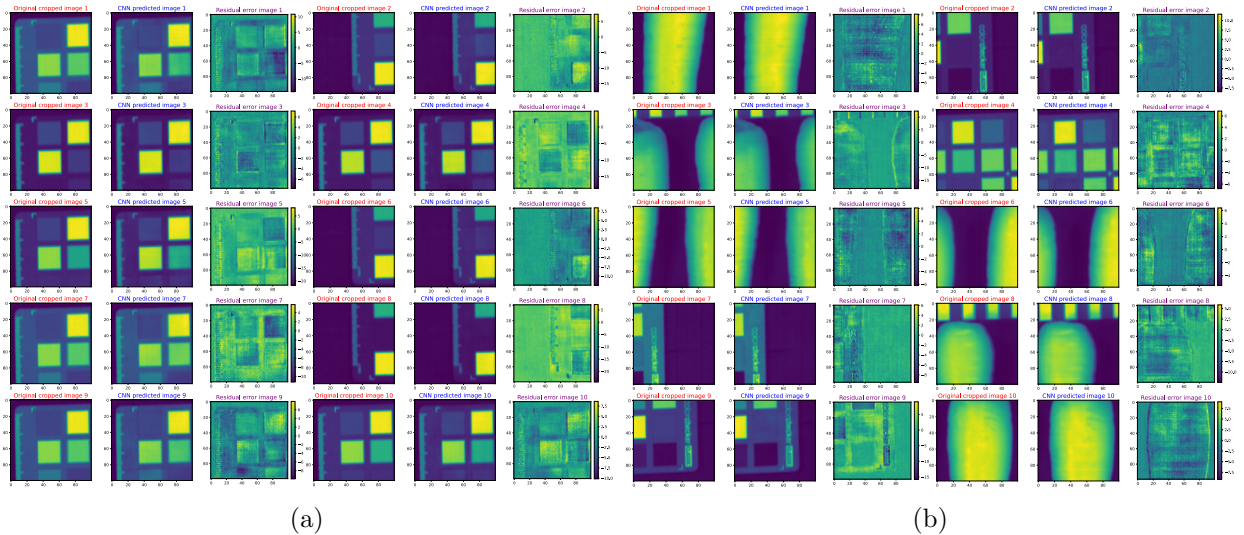


FIG. 10. (a) Similar to Fig. 5 but with 25 spectral channels. (b) Similar to Fig. 10a but with the inclusion of ColorChecker and carrot cubes. The 15th channel is shown here.

on the carrot images. Note that in light of the complexity of the model and hence a very time-consuming training process we train the model only for 25 epochs in both cases as opposed to 40 epochs in the case of 5 spectral channels. It is expected that the performance will increase with more epochs and might potentially match the previous results of 5-channel outputs with $MSE \sim 1$.

Finally, it is worth mentioning that a forward pass through the network (making a prediction) takes only 13 ms on average. It implies the network is capable of carrying out the reconstruction of 3-D data cubes *on the fly* while a CTIS camera is taking images. In this way, the subsequent data analyses based on the reconstructed cubes can also be executed in real-time and provide immediate feedback on the system; for instance, on how the deployment of the CTIS camera or the imaged object should be adjusted.

| | MSE | MAE |
|--|-------------------|-------------------|
| ColorChecker training set | 5.32 | 1.56 |
| ColorChecker test set | 5.69 | 1.59 |
| ColorCheckers + carrots training set (ColorCheckers, carrots) | 4.82 (5.33, 4.52) | 1.45 (1.55, 1.37) |
| ColorCheckers + carrots test set (ColorCheckers, carrots) | 5.03 (5.59, 4.28) | 1.48 (1.58, 1.35) |

TABLE II. Residual errors on the entire training and test datasets from the ColorChecker only and from the ColorChecker plus carrots in the case of 25 channels.

V. CTIS EXPECTATION MAXIMIZATION RECONSTRUCTION

In this Section, we compare the CNN approach with the standard expectation maximization (EM) algorithm [25], utilized in the CTIS reconstruction. We begin with the creation of a system matrix followed by the cube reconstruction using the EM algorithm. We shall see that the CNN method has a better performance in reproducing hyperspectral cubes than the EM algorithm, and has a shorter process time when it comes to cube reconstruction.

A. System matrix generation and EM

To investigate the performance of the network relative to the standard reconstruction approach, an equivalent CTIS simulation is performed. The simulation is based on the standard approach to reconstruct a hyperspectral cube from an acquired CTIS image, which assumes that the system is described by the linear imaging equation [16]:

$$\mathbf{g} = \mathbf{H} \mathbf{f} \quad (2)$$

where \mathbf{g} is the vectorized $q \times q$ CTIS image⁵ with $q = 3x + 4b$, \mathbf{H} is the $q^2 \times r$ system matrix and \mathbf{f} is the vectorized hyperspectral cube with $r = x \cdot y \cdot b$ voxels, where x, y and b denote the two spatial dimensions and spectral channels, respectively. The system matrix \mathbf{H} maps the sensitivity of the i -th voxel in \mathbf{f} to the j -th pixels in \mathbf{g} – corresponding to the five projections shown in Fig. 3b. The system matrix \mathbf{H} is constructed by assuming spatial shift-invariance and an ideal CTIS, i.e. each voxel in \mathbf{f} is projected once into each diffraction order. Spatial shift-invariance assumes that shifting a voxel by a given distance within the hyperspectral cube yields a CTIS image in which the corresponding pixels in the zero- and first diffraction orders are shifted by the same distance in the same direction. Thus, the i -th voxel, f_i , is projected onto a $q \times q$ CTIS image, which is vectorized and arranged as columns in \mathbf{H} . This process is repeated for all voxels in \mathbf{f} until \mathbf{H} has been completely constructed. Thus, each column in \mathbf{H} only has five nonzero elements corresponding to the five projections, which leads to the natural implementation of \mathbf{H} as a sparse matrix since its sparsity is $(q^2 - \text{nonzero elements})/q^2 = (400^2 - 5)/400^2 = 0.99997$.

⁵Namely, \mathbf{g} is a column vector with q^2 elements.

To effectively reconstruct the hyperspectral cube \mathbf{f} from an acquired CTIS image \mathbf{g} requires solving Eq. (2) through the inversion of the system matrix \mathbf{H} . However, since \mathbf{H} is noninvertible, the iterative EM algorithm is utilized to obtain \mathbf{f} instead. The EM algorithm consists of an expectation and a maximization step. First, an estimated CTIS image $\hat{\mathbf{g}} = \mathbf{H}\hat{\mathbf{f}}^{(k)}$ is computed in the expectation step. In the subsequent maximization step, a correction factor for every voxel in the estimated hyperspectral cube $\hat{\mathbf{f}}^{(k)}$ is computed as a back-projection of the ratio of the captured and estimated CTIS image and normalized by the summed rows of \mathbf{H} . All in all, we have:

$$\hat{\mathbf{f}}^{(k+1)} = \frac{\hat{\mathbf{f}}^{(k)}}{\sum_{i=1}^{q^2} H_{ij}} \odot \left(\mathbf{H}^T \frac{\mathbf{g}}{\mathbf{H}\hat{\mathbf{f}}^{(k)}} \right) \quad (3)$$

where k is the iteration index, $\hat{\mathbf{f}}^{(k)}$ is the k -th estimate of the hyperspectral cube, $\sum_{i=1}^{q^2} H_{ij}$ is the vectorized summation of rows in \mathbf{H} , \mathbf{H}^T is the transposed system matrix and \odot denotes the Hadamard or element-wise product. Notice, that Eq. (3) combines the expectation and maximization steps into a single step.

The algorithm is typically initialized with either $\hat{\mathbf{f}}^{(0)} = \text{ones}(r, 1)$ [26] or $\hat{\mathbf{f}}^{(0)} = \mathbf{H}^T \mathbf{g}$ [8]. The latter is assumed in this work. As 10-30 EM iterations are typically required [14], we carry out 20 iterations. Both the construction of \mathbf{H} and reconstruction of \mathbf{f} are implemented in MATLAB with the help of built-in sparse matrix manipulations.

B. Sparse EM predictions

The reconstruction algorithm requires no training data, and therefore, both the training and unseen data are reconstructed. From the data, only 2000 CTIS images have been chosen since the EM algorithm is run on a regular laptop equipped with an 11th Gen Intel® Core™ i7-1165G7 2.80 GHz CPU. The original and predicted channels as well as the residual error for the ColorChecker and carrots are shown in Fig. 11a and Fig. 11b, respectively. Similar rectangular reconstruction artifacts as seen in Fig. 10a and Fig. 10b are also visible for the EM reconstructed channels. The average computation time for 20 EM iterations over the 2000 hyperspectral cubes is measured to be 94.7 ± 3.5 ms, where the uncertainty indicates the standard deviation of the measured computation times. It is slower than a forward pass in the CNN which takes 13 ms on average. We should point out that it is not a completely fair

comparison since first the network needs the time-consuming training stage⁶ before making decent predictions and second the EM algorithm is carried out on the regular laptop as opposed to the four powerful GPUs in the CNN case. However as a proof of principle study, these results demonstrate the potential of the CNN approach on deciphering CTIS images on the fly.

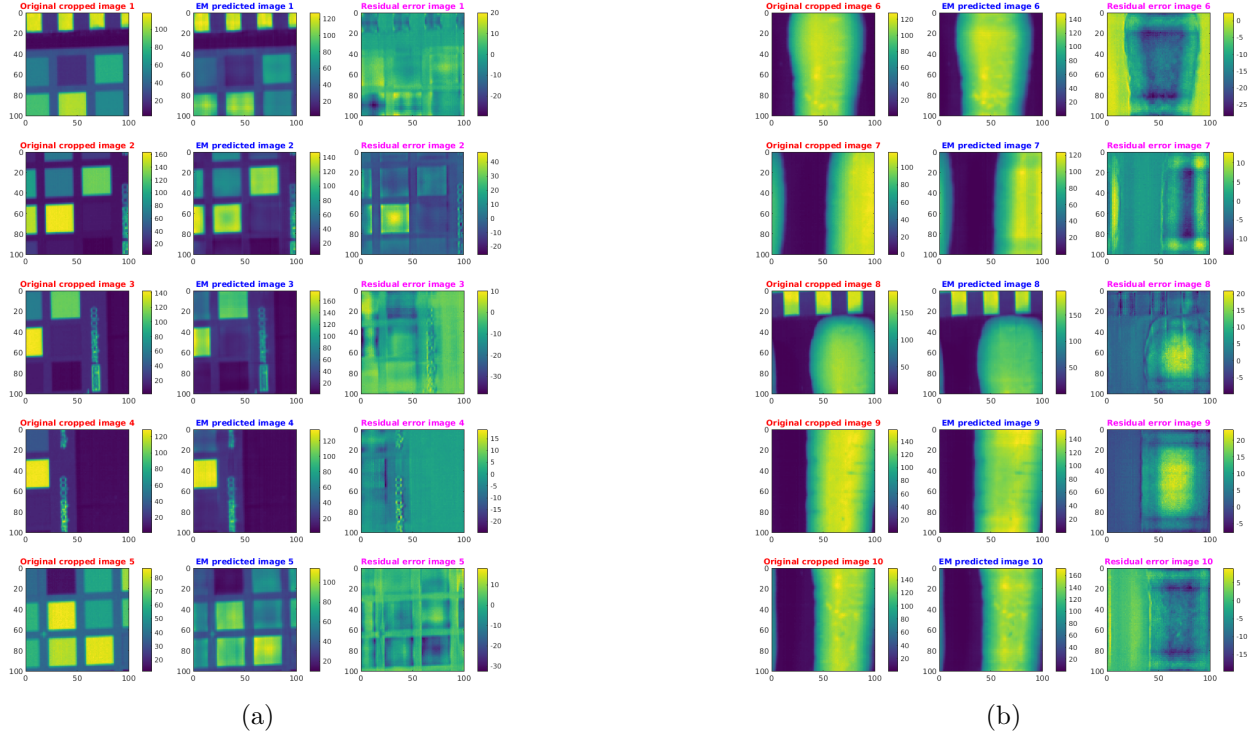


FIG. 11. Comparison of original (left column), reconstructed (central column) and residual (right column) spectral channel 15 from $100 \times 100 \times 25$ hyperspectral cubes for (a) the ColorChecker and (b) carrots based on the sparse EM reconstruction algorithm.

The mean MSE and MAE for all images are calculated and displayed in Table III: For the ColorChecker, we obtain MSE and MAE of 55.50 and 4.62, respectively, which are significantly higher than those of the networks in Table II. Similarly, the MSE and MAE for the carrots are computed to be 130.64 and 6.62, respectively. The significantly larger errors for carrots relative to the ColorChecker are due to the higher degree of spatio-spectral multiplexing for the carrots. In other words, there is less spatial separation between regions of different spectral signatures compared to the ColorChecker with separated square regions which eases the reconstruction [27, 28]. Surprisingly, this issue does not happen to the

⁶It takes around three days to train the first CNN with five spectral channels and nearly two weeks for the second CNN of 25 spectral channels.

CNNs.

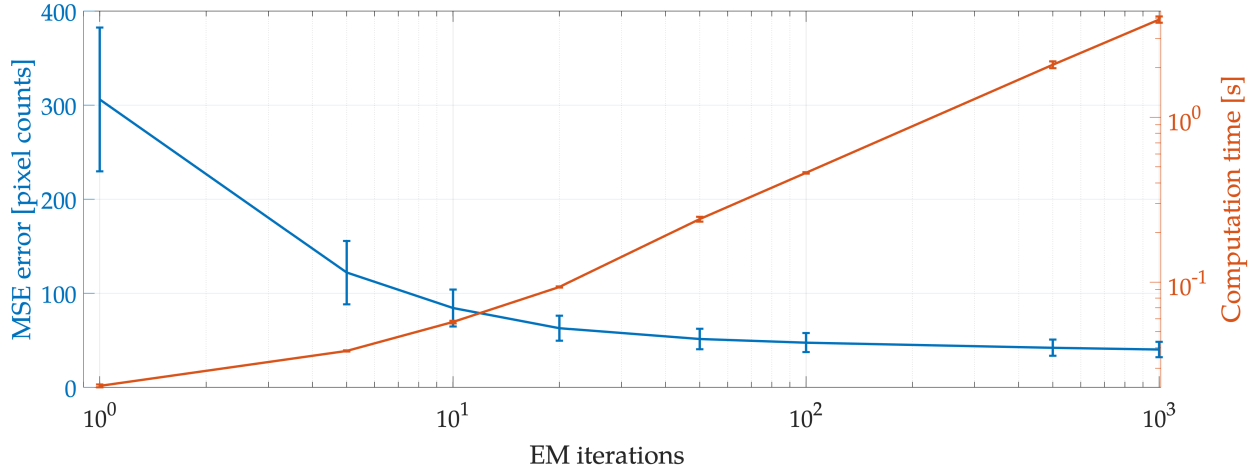


FIG. 12. The MSE and computation time for the EM algorithm as a function of EM iterations. The computed values and error bars correspond to the mean and standard deviation of 20 randomly chosen hyperspectral cubes, respectively. Again, the EM algorithm is executed on the regular laptop.

It should be noted, that both the MSE and MAE decrease asymptotically while the computation time increases linearly as the number of EM iterations increases: Fig. 12 shows the MSE and computation time for 1, 5, 10, 20, 50, 100, 500 and 1000 EM iterations. The computed values and error bars correspond to the mean and standard deviation of 20 randomly chosen hyperspectral cubes, respectively. The computation times are shown in a log-log plot since one and 1000 EM iterations take 23 ms and 3.92 s, respectively. In this work, 20 iterations have been assumed, abiding by the practice despite better performance with more iterations – going from 20 to 1000 iterations, the MSE decreases by 36 % but the computation time unfortunately increases by a factor of ~ 42 .

| | MSE | MAE |
|--------------|--------|------|
| ColorChecker | 55.50 | 4.62 |
| Carrots | 130.64 | 6.62 |

TABLE III. The mean MSE and MAE for 2000 reconstructed $100 \times 100 \times 25$ hyperspectral cubes of the ColorChecker and carrots using the EM algorithm with 20 iterations.

VI. CONCLUSIONS

The CTIS [6–8] is a non-scanning snapshot hyperspectral imaging system. A CTIS image contains a central zeroth-order undiffracted image surrounded by four first-order diffracted images. Different algorithms [14–16] are used to convert multiplexed 2-D CTIS images into 3-D hyperspectral cubes, which are easier to visualize and analyze. A CTIS camera is, however, portable and cheaper than hyperspectral imagers such as pushbroom and has a wider range of applications. However it is necessary to develop fast and reliable image reconstruction algorithms as existing ones are often prone to long reconstruction time and mediocre precision for hyperspectral cubes with a large number of spectral channels.

In this study, we propose a novel reconstruction method based on CNNs where the networks consist of five branches of convolutional layers, which allow such fast and reliable predictions. This method imitates decision tree ensembles, where a group of weak learners work together to form a strong learner. As a proof of concept, we start with a simple case where the network is required to decipher CTIS images of the ColorChecker with five spectral channels and pixel values range from 0 to 255. The average errors of MSE (MAE) summarized in Table I are around (below) one for both the training and test datasets. It should be noted that the test data is created by completely distinct hyperspectral cubes from those of the training data. These results demonstrate that the network can deliver satisfactory performance and generalize well to new (unseen) data of same basic type. CTIS images of carrots are then included in the training sets to demonstrate that the network can simultaneously manage different kinds of images and in particular images of direct relevance to industrial applications of CTIS imaging, such as frost damage detection in vegetables.

However, some of the relevant industrial applications of CTIS will require more than five spectral channels and we therefore studied the more challenging scenario with 25 spectral channels. Decent levels of precision, collected in Table II, with MSE (MAE) ~ 5 (1.6) are obtained and the forward pass time (the time it takes to make a prediction) takes only 13 ms. It underscores the potential of applying CNN to real-time reconstruction of hyperspectral cubes with simultaneously captured CTIS images. Finally, we have shown for one of the standard reconstruction methods, the EM algorithm, that the corresponding residual errors are much larger (by more than a factor of 10; see Table III) and the reconstruction time is also longer, depending on the number of EM iterations and computational power available.

To summarize, we have demonstrated that CNNs can be used to convert CTIS images into a hyperspectral cube in an efficient and precise manner. Our work lays the foundation for future studies on network architecture and optimization with the goal of realizing fully automated and versatile CNNs for reconstruction of hyperspectral cubes on the fly which will warrant a broad range of applications where real-time 2-D spectroscopy is in demand.

ACKNOWLEDGMENTS

MTF and WCH acknowledge partial funding from the Independent Research Fund Denmark, grant number DFF 6108-00623, The Villum Foundation and a CenSec grant funded by The Danish Ministry of Higher Education and Science (CenSec). This work was performed using the [UCloud](#) computing and storage resources, managed and supported by eScience center at SDU.

-
- [1] A. F. Goetz, G. Vane, J. E. Solomon, and B. N. Rock, [Science](#) **228**, 1147 (1985), <https://science.sciencemag.org/content/228/4704/1147.full.pdf>.
 - [2] N. Keshava, [42](#), 1552.
 - [3] H. Lee, M. S. Kim, Y.-R. Song, C.-S. Oh, H.-S. Lim, W.-H. Lee, J.-S. Kang, and B.-K. Cho, [97](#), 1084.
 - [4] Y.-Y. Pu, Y.-Z. Feng, and D.-W. Sun, [14](#), 176.
 - [5] B. Boldrini, W. Kessler, K. Rebner, and R. Kessler, [Journal of Near Infrared Spectroscopy](#) **20**, 438 (2012).
 - [6] T. Okamoto and I. Yamaguchi, [Opt. Lett.](#) **16**, 1277 (1991).
 - [7] T. V. Bulygin and G. N. Vishnyakov, in [Analytical Methods for Optical Tomography](#), Vol. 1843, edited by G. G. Levin, International Society for Optics and Photonics (SPIE, 1992) pp. 315 – 322.
 - [8] M. Descour and E. Dereniak, [34](#), 4817.
 - [9] B. K. Ford, M. R. Descour, and R. M. Lynch, [Opt. Express](#) **9**, 444 (2001).
 - [10] W. R. Johnson, D. W. Wilson, W. Fink, M. Humayun, and G. Bearman, [12](#), 014036.

- [11] K. Hege, D. O’Connell, W. Johnson, S. Basty, and E. Dereniak, *Proceedings of SPIE - The International Society for Optical Engineering* **5159** (2004), 10.1117/12.506426.
- [12] W. Yang, C. Yang, Z. Hao, C. Xie, and M. Li, *IEEE Access* **7**, 118239 (2019).
- [13] C. Douarre, C. F. Crispim-Junior, A. Gelibert, L. Tougne, and D. Rousseau, *Appl. Opt.* **59**, 8697 (2020).
- [14] L. White, W. B. Bell, and R. Haygood, **59**, 1.
- [15] M. D. Vose and M. D. Horton, **46**, 6498.
- [16] N. Hagen, E. L. Dereniak, and D. T. Sass, pp. 666103–666103–11.
- [17] Y. LeCun, B. Boser, J. S. Denker, D. Henderson, R. E. Howard, W. Hubbard, and L. D. Jackel, *Neural Computation* **1**, 541 (1989).
- [18] Y. Lecun, L. Bottou, Y. Bengio, and P. Haffner, *Proceedings of the IEEE* **86**, 2278 (1998).
- [19] <https://www.tensorflow.org/>.
- [20] <https://keras.io/>.
- [21] G. Van Rossum and F. L. Drake, *Python 3 Reference Manual* (CreateSpace, Scotts Valley, CA, 2009).
- [22] L. Breiman, *Machine Learning* **45**, 5 (2001).
- [23] J. H. Friedman, *The Annals of Statistics* **29**, 1189 (2001).
- [24] D. P. Kingma and J. Ba, arXiv e-prints , arXiv:1412.6980 (2014), [arXiv:1412.6980 \[cs.LG\]](https://arxiv.org/abs/1412.6980).
- [25] L. A. Shepp and Y. Vardi, **1**, 113.
- [26] D. W. Wilson, P. D. Maker, and R. E. Muller, pp. 184–193.
- [27] N. Hagen, E. L. Dereniak, and D. T. Sass, in *Imaging Spectrometry XI*, Vol. 6302 (International Society for Optics and Photonics) p. 63020L.
- [28] N. Hagen and E. L. Dereniak, **47**, F85.